

# Hybrid Sensor for Joint Space Domain Awareness and Lunar Surface Intelligence

Anna M. Lawitzke, Jeffrey E. Van Cleve, James Contreras, David Ramirez, Timothy Finch, Jeremy Correa  
*Ball Aerospace*

## ABSTRACT

Last year we discussed a hybrid sensor system which can perform both lunar surface intelligence (LUNINT) and Space Domain Awareness (SDA) missions using two sensors in complementary lunar orbits, each of which has a focal plane array (FPA) which can stare into deep space for long integration times for SDA and can be reconfigured for high line rate virtual Time Delay Integration (TDI) imagery of the lunar surface when near periapsis [1]. We introduced requirements for both SDA and LUNINT missions, in particular the target visual magnitude and revisit rate for SDA and the ground sampling distance for LUNINT, sketched out first-order optical parameters for the telescope, and examined cislunar space volume and lunar surface access for 6 different 2-vehicle constellations. In this paper, we apply the design and concept of operations (CONOPS) options introduced in [1] to

- Develop a hybrid FPA architecture road map for consultation with FPA vendors and Ball's Detector Technology Center
- Develop a semi-analytic joint merit function which balances SDA and LUNINT performance, for quick concept and parameter set evaluation before design work
- Spot-validate merit function against detailed mission analysis
- Develop a telescope design which can collect enough photons to quickly sweep the SDA volume, has small enough pixels to usefully resolve targets on the lunar surface, has good straylight rejection, and is buildable and agile.
- Build on last year's cislunar volume access study by assessing SDA performance against a target deck which includes objects at the Lagrange points, in transit between the Earth and Moon, and in both elliptical and circular lunar orbits with low periapsis consistent with takeoff/landing trajectories or surface-observing sensors. The target radiometric model is a Lambertian sphere.
- Build on the surface access component of last year's study by including surface illumination as a condition for access and calculating the distribution of gap times over the year for a surface target deck that includes objects near the lunar poles including permanently shadowed regions (PSRs). The PSR interior illumination model and thus the threshold geodetic sun angle as a function of topography is developed in a companion paper at this conference [2]
- Present an observing timeline showing when and where the sensor is looking into space or at the lunar surfaces function of orbital phase, for the optimal orbit to illustrate the concept of operations.

## 1. INTRODUCTION: Exploration of Cislunar Mission Space

### 1.1 Overview of Cislunar Domain

While SDA has historically been practiced in the LEO to GEO domains, the growing quantity of missions and traffic to cislunar space drives the importance and need for above-GEO (XGEO) SDA. As an example, NASA's ARTEMIS and Commercial Lunar Payload Services (CLPS) programs, AFRL's CHPS, and the future planned Chinese activities will lead to numerous assets and rocket bodies launched into the Earth-Moon gravitational corridor in the coming years. Cislunar SDA and Lunar Intelligence (LUNINT) systems will be critical to protecting and maintaining operational confidence for safe transit and situational awareness.

LEO satellite systems will be insufficient to monitor the vastness of XGEO space. Even Cislunar space traffic management (STM) requires a higher sensitivity optical system than SDA in GEO due to the long ranges, larger search volumes, and complex cislunar orbits. Observability in the cislunar corridor is also challenging and limited due to lunar, earth, and solar angular exclusion zones. Because of this, one or more low lunar orbiters are required to completely cover the  $4\pi$  steradian cislunar regime by tracking low lunar orbit satellites and as well as periodic imagery to detect changes on the lunar surface.

## 1.2 Why combine SDA with LUNINT?

In the context of the broad cislunar space discussed above, we propose a lunar orbiter that provides both Lagrange-zone SDA coverage of the cone of shame and observations of the lunar surface from orbits which at least at periapsis pass close enough to the surface to detect and resolve meter-size objects. While this mission could be accomplished using two payloads on a single lunar orbiter, we propose using a single payload to save cost. A merit function will be introduced to aid in optimizing the lunar orbit to meet the mission preference between SDA and LUNINT. A case study with resulting payload and performance will also be presented assuming equal weighting between the SDA and LUNINT missions.

This paper is related to these companion papers at this conference which explore other aspects of cislunar SDA:

- Awareness of near-Moon space and the interior of Shackleton Crater from sites on the lunar surface which complements the awareness of the surface as seen from space discussed in this paper. [3]
- Awareness of the surface as seen from above which complements the awareness of space as seen from the surface discussed in this paper [2]

## 2. NOMENCLATURE

Table 1: Variable descriptions and units. Orbital element values for orbit selected using the merit function (§3)

Variable	Description	Value	Unit
$t$	Time from periapsis	varies	minutes
$\theta$	angle from periapsis	varies	“anomaly”, radians
$P$	Period, min	146.6	minutes
$\epsilon$	eccentricity	0.17	unitless
$a$	semimajor axis	2126	km
$h$	Altitude	varies	km
$h_{\min}$	Periapsis Altitude (periselene)	28	km
$h_{\max}$	Apoapsis Altitude (apselene)	750	km
$r(\theta)$	Orbit radius	varies	km
$R_M$	Radius of Moon	1737	km
<b>GSD</b>	Ground Sample Distance	0.5 - 2.0 m	m or inches (see notes in text)
<b>IFOV</b>	Instantaneous field of view	18.08	$\mu$ rad
$T_0$	Periapsis epoch	free parameter	Julian Date
$W$	RAAN	free parameter	degrees
$\omega$	Argument of periapsis	270	degrees
$\Omega$	Optical field of view	9	square degrees
$\Lambda$	Longitude	from orbit	degrees
$\lambda$	Optical wavelength	0.4-0.9	$\mu$
$f_{LT}$	LUNINT merit function		unitless
$XT$	Cross-track swath width	4.24	degrees
$b_{XT}$	LUNIT Normalizing factor based on cross-track swath width		unitless
$\phi$	Latitude, sub-spacecraft		degrees
$\phi_{\text{polar}}$	Degrees away from poles		degrees
$b_{\Omega}$	SDA Normalization factor based on FOV area		Square degrees
$f_{LS}$	LUNINT preference factor which is a subjective weighting of the importance of LUNINT vs SDA		unitless
$\beta_m$	Lunar limb avoidance angle	15	degrees
$\gamma_m$	Zenith Angle		degrees
$h(\theta)$	Altitude as a function of $\theta$		km
$\Omega_{\text{SDA}}$	Fraction of the sky instantaneously visible for SDA		unitless
$K$	time-average functional		unitless

$f$	Joint Merit function		unitless
$b_i$	Normalizes integration time		unitless

Note: Case Study values for best orbit shown in value column

### 3. MISSION ARCHITECTURE CONSIDERATIONS

Using a single focal plane and telescope to perform two missions while saving cost requires a joint merit function which weights the component merit functions of the LUNINT and SDA missions. Otherwise, optimizing performance for both missions independently would drive cost up and make the system more complex and difficult to build. We develop a semi-analytic merit function to guide the selection of parameters for modeling with numerical tools (STK), help explain the results, and understand the meta-question of what makes a good merit function, which depends on the interests and values of the customer. For example, if the end user has no interest in one of the two missions, the hybrid concept is moot, and we optimize performance vs. cost for the preferred mission. To demonstrate our methods in a succinct manner in this paper, we reduce the problem dimensionality by fixing optical parameters (FOV, IFOV, number of pixels) and adjusting the orbit periapsis and apoapsis. In future work, we will examine optical parameters vs. cost. Variables are all defined in Section 2, Table 1.

Both LUNINT and SDA merit functions are based on the analytic solution of a Keplerian orbit [4, Eq. 8.41]

$$t(\theta) = \frac{P}{2\pi} \left[ 2 \tan^{-1} \left( \sqrt{\frac{1-\varepsilon}{1+\varepsilon}} \tan \frac{\theta}{2} \right) - \frac{\varepsilon \sqrt{1-\varepsilon^2} \sin \theta}{1+\varepsilon \cos \theta} \right] \quad (1)$$

$$r(\theta) = \frac{a(1-\varepsilon^2)}{1+\varepsilon \cos \theta} \quad (2)$$

$$h = r(\theta) - R_M \quad (3)$$

Our calculations use Ground Sample Distance (GSD) in meters but historically the GEOINT community has referred to GSD in inches so one must take care with numerical values from the literature.

$$\text{GSD}(\theta) = h(\theta) * \text{IFOV} \quad (4)$$

Instantaneous performance metrics represented by a function  $g(r(\theta), \theta)$  are then numerically time-averaged over the orbit to obtain the “Keplerian average” component merit functional

$$K(g(r(\theta), \theta)) = \frac{1}{P} \int_{-\pi}^{\pi} g(r(\theta), \theta) \frac{dt}{d\theta} d\theta \quad (5)$$

Where the merit function is normalized such that  $K(1) = 1$  for a circular orbit where  $t = \frac{P\theta}{2\pi}$ .

For LUNINT, where merit functions depend on the Moon location being observed, the orbit plane coordinates in **Error! Reference source not found.** are transformed to LUNINT ground track coordinates (sub-spacecraft point latitude  $\phi$  and longitude  $\Lambda$ ) using the equations in [5] to convert perifocal to planetocentric coordinates given the periapsis epoch, RAAN, and argument of periapsis. Note that we use

- $W$  for RAAN so as not to confuse it with the optical FOV  $\Omega$
- $\Lambda$  for longitude to not confuse it with optical wavelength  $\lambda$ .

The instantaneous metric for LUNINT is based on the National Imagery Interpretability Scale (NIIRS) General Image Quality Equation General Image Quality Equation (GIQE) v. 5 [6], for which the sharp image high SNR limit is

$$\text{NIIRS} = 9.7 - 3.32 \log_{10}(\text{GSD}) \cong 9.7 - \log_2(\text{GSD}) \quad (6)$$

So that a NIIRS difference of 1.0 corresponds to a factor of 2 change in GSD[6]. Note that GSD is in *inches* in the above equation. Clearly, NIIRS 9 image (detect spikes in railroad ties) is more than 3x as valuable as a NIIRS 3 image (detect trains), so we take a cue from the  $\log_2$  term and set the instantaneous local value of a NIIRS image to be proportional to  $2^{\text{NIIRS}}$  or  $\sim 1/\text{GSD}$  and the LUNINT merit function with GSD now in meters. We also define a latitudinal step function,  $c(\phi)$ , which activates when sufficiently close to the poles, typically poleward of  $\phi_{\text{polar}} = 5$  degrees as

$$c(\phi) = \begin{cases} 0, & |\phi| < \phi_{\text{polar}} \\ 1, & |\phi| \geq \phi_{\text{polar}} \end{cases} \quad (7)$$

$$f_{LT} = \left( \frac{XT}{b_{XT}} \right) \frac{K(c(\phi(\theta)))}{\text{GSD}(\theta)} \quad (8)$$

Here,  $f_{LT}$  captures the notion that wider XT is better, the normalization factor  $b_{XT}$  is set equal to the XT width of our design ( $4.24^\circ$ ) since  $f_{LT}$  will be in turn multiplied by an arbitrary “LUNINT preference factor”  $f_{LS}$  (see below) and our purpose here is to demonstrate use of the merit function along the dimensions of orbit periapsis and apoapsis. Future work will tackle the use of the merit function along dimensions like XT, to be divided by a cost function of XT and other optical parameters to find an optimum.

If one is equally interested in all-sky SDA and equally interested in the entire lunar surface for LUNINT, one is *still* better off optimizing for one or the other missions. An interesting result emerges, however, if the LUNINT mission is only important within a certain latitude radius ( $\phi_{\text{polar}} < 10^\circ$  or so). Then, there is an orbit which is least non-optimum in the sense of accommodating a wide range of preferences for SDA vs. LUNINT among end users.

The instantaneous SDA metric is the fraction of the sky visible, excluding the lunar disk and the lunar limb avoidance angle,  $\beta_m$ , which is set to 15 degrees in the optical design and radiometry (§3), as shown in Fig. 1.

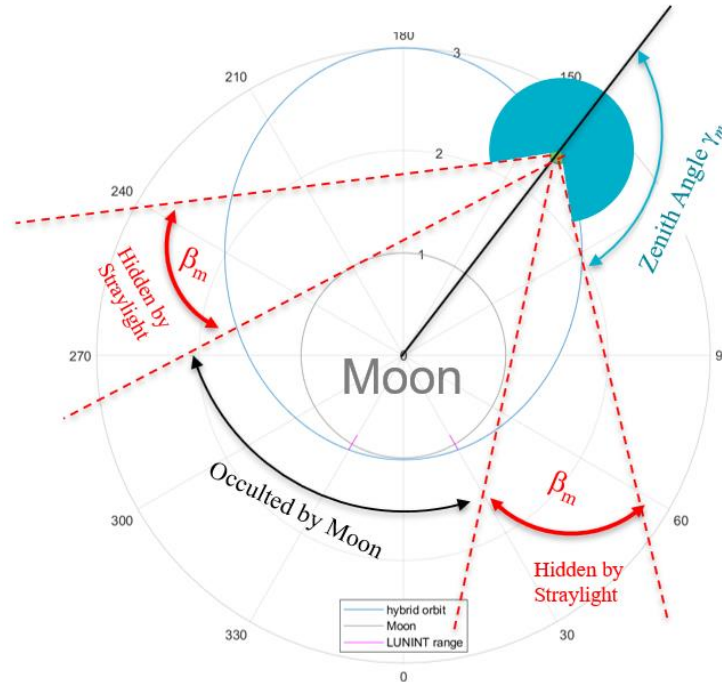


Fig. 1: Instantaneous sky visible for the SDA mission at a given orbit point, for an example hybrid orbit evaluated with the merit function.

The zenith angle in degrees at the edge of the lunar limb avoidance zone is then

$$\gamma_m = 90^\circ + \cos^{-1} \frac{R_M}{R_M + h(\theta)} - \beta_m \quad (10)$$

The fraction of lunar sky instantaneously visible for SDA is

$$\Omega_{SDA} = \frac{(1 - \cos(\gamma_m))}{2} \quad (11)$$

and the SDA merit function is

$$f_{SDA} = K(\Omega_{SDA}) \quad (12)$$

The instantaneous merit for LUNINT and SDA is shown in Fig. 2.

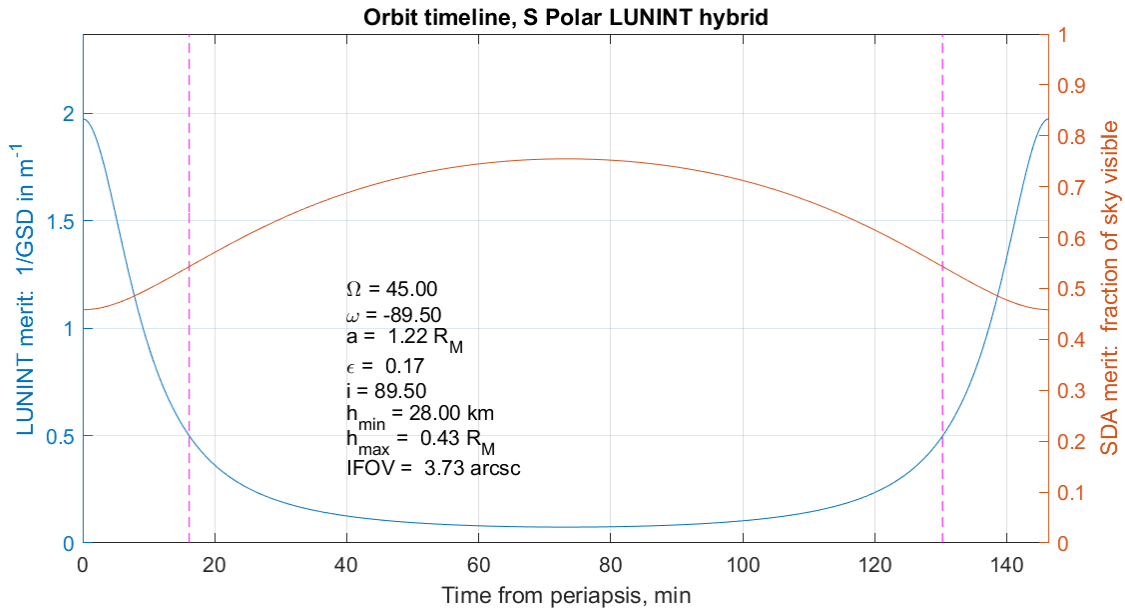


Fig. 2: LUNINT and SDA instantaneous merit timeline for the best case identified in Table 1. Magenta lines show the largest useful GSD of 2.0 m [2]

The joint merit function is then a normalized sum of LUNINT and SDA as

$$f = \frac{f_{LS} \cdot XT \cdot f_{LT}}{b_{XT}} + \frac{(1 - f_{LS}) \cdot \Omega_{FOV} \cdot b_t}{b_{\Omega} \cdot t_{dwell}} \cdot f_{SDA} \quad (13)$$

The LUNINT vs SDA preference factor,  $f_{LS}$ , is a subjective weighting of the importance of LUNINT vs SDA.

- $\Omega_{FOV}$  = solid angle of FOV in square degrees. Rationale: merit proportional to area searched. As with XT, the normalization constant,  $b_{\Omega}$ , is taken to match our design of 9 square degrees.
- $t_{dwell}$  = total integration time is s for benchmark target + slew-settle time. Rationale: merit proportional to camera speed (inverse of dwell time to fixed SNR).
- Numerical prefactors so parenthetical values = 1.0 in baseline design

Obviously, one might have exceedingly high LUNINT merit by flying exceedingly close to the ground! However, based on LRO experience flying at altitudes lower than 20 km requires considerable attention and station-keeping to avoid crashing into the topography, while GSDs < 0.4 m will require frame rates > 4 kHz, which would invalidate the FPA CONOPS in the next section. For margin, we set the lowest altitude to 28 km and the minimum nadir GSD to 0.5 m, thus setting our IFOV to 18 mrad (§3).

Table 2 shows the interesting result. For any given preference factor, one is led to either a circular Low Lunar Orbit (LLO) or a highly-eccentric lunar orbit (HELO), or there is no obvious best orbit. However, over the entire range of preferences, the 750 km altitude orbit is the least distant from acceptable performance (shown in green in the table, defined as 10% decrease in joint merit from the maximum). Hence, we adopt this best (least sub-optimal) orbit as our baseline. We do not show higher periapsis results since the higher periapsis substantially degrades LUNINT while having only small benefit for SDA.

We expect that this mission, like Lunar Reconnaissance Orbiter (LRO) before it, will have to carry significant fuel for orbit maintenance, given the general instability of lunar orbits below 100 km [7] altitude and perhaps for orbit-change maneuvers in response to events in cislunar space. As an example, LRO was injected into Trans Lunar Injection (TLI) and carried enough fuel for Lunar Orbit Insertion (LOI) and >230 m/s orbit maintenance and maneuvers. It is still operating 13 years later in a <30 km x 156 km S. pole periapsis elliptical orbit, and we expect the Hybrid vehicles to have similar station-keeping requirements. The Hybrid mission could also take advantage of frozen orbits as discussed by [7] to considerably reduce station-keeping at some cost in observing merit. See Osterman+ for more about LUNINT orbits and observation planning.

Table 2: Component and joint merit vs apoapsis altitude for 28 km periapsis for a range of LUNINT/SDA preferences. Green fill indicates merit score is within 10% of the maximum for that preference. The 750 km apoapsis altitude is the best (least disagreeable) for a range of preference weightings

components						joint merit ( <i>f</i> )				
Altitude – <i>h</i>		SMA	e	LUNINT	SDA	Lunar Preference				
Periapsis (km)	Apoapsis (km)	(km)	deg	$\phi$	<W>	0	0.25	0.5	0.75	1
28	30	1,766	0.001	1.827	0.459	0.459	0.801	1.143	1.485	1.827
28	50	1,776	0.006	1.816	0.473	0.473	0.809	1.145	1.480	1.816
28	100	1,801	0.020	1.771	0.499	0.499	0.817	1.135	1.453	1.771
28	204	1,853	0.047	1.737	0.538	0.538	0.838	1.138	1.437	1.737
28	500	2,001	0.118	1.594	0.606	0.606	0.853	1.100	1.347	1.594
28	750	2,126	0.170	1.523	0.643	0.643	0.863	1.083	1.303	1.523
28	1,000	2,251	0.216	1.433	0.671	0.671	0.862	1.052	1.243	1.433
28	1,737	2,620	0.326	1.279	0.726	0.726	0.864	1.003	1.141	1.279
28	3,474	3,488	0.494	1.037	0.790	0.790	0.852	0.914	0.975	1.037
28	5,211	4,357	0.595	0.886	0.822	0.822	0.838	0.854	0.870	0.886
43	204	1,861	0.043	1.126	0.545	0.545	0.690	0.836	0.981	1.126

#### 4. HYBRID SENSOR DESIGN FEATURES

As discussed in [1], given our  $m_s = 16.9$  reference target and mean sweep rate in square degrees/s we are led to a 30 cm aperture telescope with an SDA FOV of 9.0 square degrees and a LUNINT GSD of 0.5 m at nadir periapsis, a requirement discussed in more detail in [2]. The orbital constraints in the preceding section then give an IFOV of 18  $\mu$ rad, and the SDA FOV tells us there must then be 8 Mpix. The SDA mission is only weakly affected by the aspect ratio of this array, while the LUNINT mission benefits from wider cross-track (XT) dimension until it becomes optically difficult to make sharp images at the end. Early iteration with optical design led us to consider at 4k column x 2 k row FPA, corresponding to a 2.0 km swath width at nadir periapsis. The pixel pitch is 18  $\mu$ m in order to support the optical design (that is, not require an  $F/\# < 3$  given the aperture and IFOV).

The effective line rate of the sensor is then independent of optical design details and only weakly dependent on the orbit since the periapsis velocity varies between 1.7 and 2.3 km/s. In order not to blur the image, data must be read out at velocity/GSD Hz, or 3.4 to 4.6 kHz. We adopt 4.0 kHz as a typical value. The hybrid FPA challenge is to

collect faint point source imagery for SDA using integration times between 1 and 10 s, while being able to read out data at 4 kHz for LUNINT.

There are several focal plane approaches to collecting data at this rate. Historically, the MVIC instrument on Pluto New Horizons patterned both time-delay integration (TDI) line arrays for surface imaging and framing arrays for imaging stars for navigation on the same piece of silicon. This led to some interesting crosstalk problems and is not a true hybrid in that separate detector silicon and video signal chains were used for different purposes. A modernized MVIC FPA might combine both functionalities with low read noise by adding charge instead of sampled voltages on-chip, but such a chip is speculative without substantial investment. Instead, we examined how framing FPAs could be operated so that a subset of the image – a small number of lines – can be read out at  $\geq 4.0$  kHz much faster than typical full frame rates of 60 Hz or less. The subframes are synchronously added in a dedicated FPGA Mission Data Processing (MDP) to implement digital TDI as per [1, Fig. 1]. The focal plane has low and high gain outputs, so low gain can be used for brightly illuminated parts of the Moon and high gain (low read noise) outputs can be used for SDA and LUNINT in PSRs and more general low-light conditions (Earthshine, terminator). For our radiometric modeling and CONOPS we made the FPA assumptions shown in Table 3.

Table 3: Strawman FPA for Hybrid Sensor

High/Low Gain Ratio	7		cols	4096	
Read Noise, high gain, median over pixels	33	e-	rows	2048	
Read Noise, low gain, , median over pixels	231	e-	wavelength range	0.4 - 1.0	$\mu\text{m}$
Well depth, high gain	90	ke-	Quantum Efficiency (QE)	80%	
Well depth, low gain	630	ke-	Full frame rate	30	Hz
Dark current	20	e-/s	Subframe rows	16	
pixel pitch	18	$\mu\text{m}$	Subframe rate	3840	Hz

The subframe rate used for LUNINT is naïve in the sense that it is the full-frame rate divided by the fraction of rows read. On the other hand, a 60 Hz full-frame rate is not unusual, so there is some margin. If the Hybrid concept elicits funded interest, a sketch of our roadmap is to contact vendors to discuss subframe readout timing overheads, latent images, effective integration time, and modest redesign of the read-out integrated circuit (ROIC) to for 4k x 2k format. We would also improve our understanding of well depth vs. read noise at the two gain settings, instead of the naïve assumption that the noise in  $\mu\text{V}$  is the same for both outputs and thus the noise in e- is inversely proportional to gain.

The telescope itself has been designed to reject most stray light when the boresight is more than 15 degrees from the lunar limb, so that SDA operations can be performed over most of the sky (Section 3). The dynamic range requirement for PSRs is about 7,000 – see [2] for a derivation along with other detailed discussion of lunar surface radiometry and illumination models. While each gain channel of the focal plane has a dynamic range (max output/read noise) of  $\sim 3000$ , almost all scene contents can be captured by judiciously switching gains when the ground track approaches the bright crater rim. The telescope design meets the lunar limb requirement.

## 5. HYBRID TELESCOPE DESIGN

### 5.1 Optical Design and Evaluation

The dominant driving parameter for the telescope is the 30cm aperture; while it is feasible to build a refractive system at this aperture size, the higher transmission, lower complexity, lower mass and improved thermal stability of a reflective telescope makes it a more desirable choice. The next key parameter is the relatively large field of view (FOV);  $2^\circ \times 4^\circ$  exceeds the capability of most on-axis reflective forms and is large enough to suggest an architecture without an intermediate image is preferred for point spread function (PSF) quality. The next top consideration for the telescope design form selection is mass, which translates directly to telescope volume, because of its impact on mission

cost. Finally, for delivering the stray light performance needed for the LUNINT mission, minimizing the telescope volume is also suggested to allow for the maximum baffle length.

In consideration of the driving parameters, the baseline telescope is a reflective triplet (RT) utilizing freeform surface departures and a rectangular aperture, a compact form that will provide sufficient image quality over the full FOV to support both missions. Its compactness also allows for the maximum baffle length to be implemented for a given payload volume allocation, thus enabling stray light performance to be met despite this form not having a field stop. Zerodur mirrors and a composite optical bench have been selected to provide the lowest risk of unacceptable amount thermal image quality degradation over the operational environment. A CAD layout of the optical design is shown in Fig. 3. This design delivers a maximum root-mean-square wavefront error (RMSWFE) LUNINT of  $<110\text{nm}$  over the full FOV, which is RSS 12% of the wave front error (WFE) allocation to the most stringent ensquared energy (EE) requirement in the center of the FOV; this leaves substantial margin for fabrication, alignment, environmental degradation, and target range variation. Keystone distortion is  $<2\mu\text{m}$  over the LUNINT TDI region.

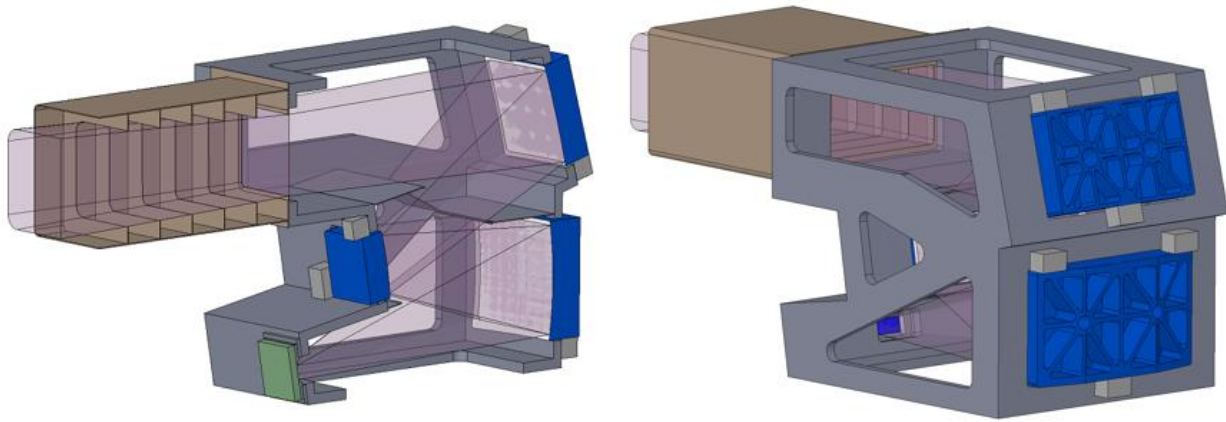


Fig. 3: CAD Layout of Freeform Reflective Triplet

For the purposes of this study, a single value conversion of the most stringent EE requirement to root-mean-square wavefront error, RMSWFE, was generated; this requirement, 58% in the LUNINT center region, refers to the spatial distribution of the PSF centered on a pixel, it does not include telescope transmission or detector QE, but it does include the impact of normalized detector QE on the diffraction PSF as a function of wavelength to accurately capture the PSF shape. Fig. 4 shows the EE as a function of RMSWFE generated by applying the 4 major 3<sup>rd</sup> order aberrations to the entrance pupil. When a detailed performance budget is derived under a formal program, the aberration mix generated by the dominant errors will be used; for this study, a combination of coma and power/astigmatism (which are nearly identical for this aperture shape) was used. Applying a modest margin to the requirement to account of the coarse nature of this conversion technique, 75% EE translated to an RMSWFE of  $\sim 300\text{nm}$ , which is the goal set for the telescope for this study.

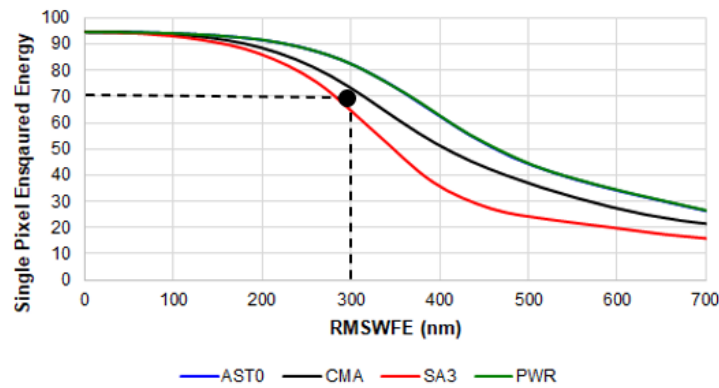


Fig. 4: EE to RMSWFE Conversion

Using a fabrication and alignment error set similar to comparable size, heritage Zerodur-composite telescopes and a relatively simple optical compensation strategy, a preliminary RMSWFE budget was constructed against the conservative scenario of needing to meet the most stringent center field requirement over the full FOV. Using analysis results (blue) for all but the final two line items (green, allocation), the preliminary budget shown in Fig. 5 demonstrates that environmental degradation (“STOP”) can be allocated nearly RSS 25% of the budget while still retaining a margin of RSS 10%. Recalling that this budget is against the center field requirement and composed of low CTE Zerodur mirrors and composite bench, the likelihood of meeting imaging performance after detailed analyses are performed is high.

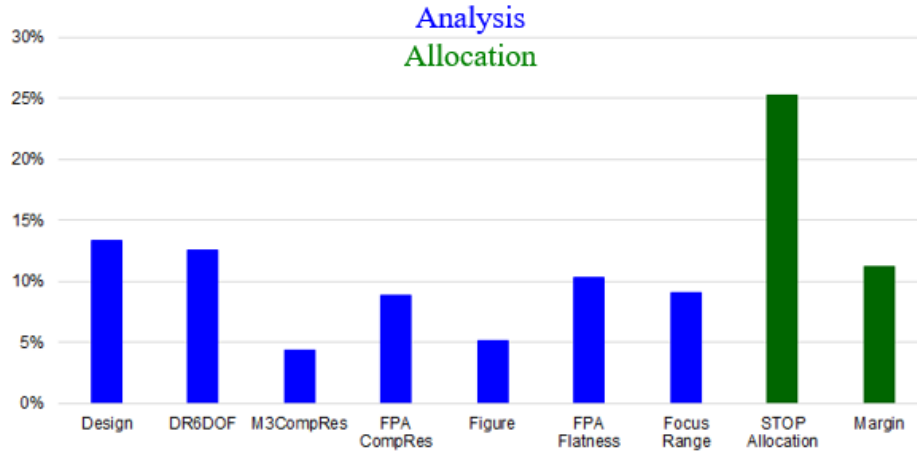


Fig. 5: Preliminary WFE Budget

Two other telescope forms, both including field stops to potentially improve stray light, were also derived. Although each was less desirable from a PSF perspective, they were also sufficiently larger volume that substantially less volume was available for the entrance baffles. As a consequence of the shorter entrance baffles, the resulting stray light results showed very little improvement over the RT, thus the simpler, lower alignment sensitivity RT was retained as the baseline.

## 5.2 Stray Light Design and Evaluation

An opto-mechanical stray light model was built to evaluate the design for feasibility against mission goals. The assumptions made in this model were chosen to ensure a design that could be manufactured safely within standard practices without driving cost. Several design levers are available should the need for higher performance arise. A lightshade was designed that implements the telescopes aperture stop and provides 6 additional vanes to support stray light performance in support of mission goals. In addition to the entrance baffle vanes, masks were included around the clear aperture of each mirror, and two baffles internal to the housing were incorporated for mitigation of unwanted sneak paths.

To enable standard machining and alignment, vanes and internal baffles were implemented with 2.5mm radial margin to design FOV footprints, and all vanes have 0.010” knife edges at the inner aperture. All mechanical surfaces were modeled as coated with Aeroglaze Z307 black paint, the BRDF of which has been well characterized by Ball. The mirror surfaces were assumed to have 30Å RMS surface roughness (using the K-Correlation model) and a particulate contamination level of CL500 EIST-STD-CC1246D (per Mie theory, using the standard particle slope of 0.926).

A reverse trace to sky analysis method was used to generate the stray light response function (Point Source Transmittance, or PST) in 2-D angle space for an on-axis 18µm pixel location. The full hemisphere log<sub>10</sub> PST mapped to a rectilinear grid is shown on the left of Fig. 6, with X and Y profiles through center shown at right. The substantial asymmetry in X and Y arises from the rectangular aperture impacting the angles at which the primary mirror can no longer be directly illuminated. Additionally, the lack of a vane at the entrance of the lightshade tube causes a secondary cliff, leading to effectively zero stray light response at very large angles from boresight.

This calculated PST is then used for mission level modeling. A MATLAB tool calculates radiance from a broad illuminated source and integrates against the PST both for the SDA lunar limb exclusion angle analysis and the LUNINT staring operation. The limb results have been incorporated directly into the radiometric performance analysis in section 7.1 and are not discussed here. The LUNINT operational conditions were evaluated at an altitude of 28km, using a crater 50x dimmer than the surrounding uniformly bright Lunar surface. This analysis yielded an imaged signal pixel on the order of 106 more counts than the stray light noise from the integrated out of field Moon, demonstrating that the surrounding illuminated lunar surface stray light signal will be negligible when imaging a dark lunar crater.

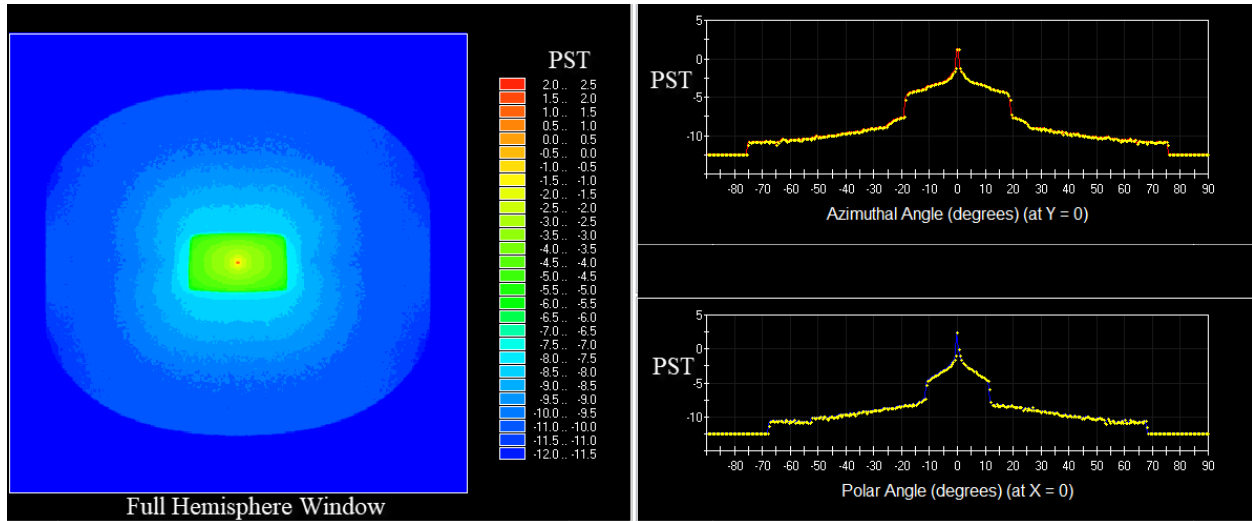


Fig. 6: Stray light response (PST)

## 6. MISSION DATA PROCESSING FOR HYBRID PAYLOAD

As discussed in [8], the distances between the Earth and the Moon are 81x more challenging than transmitting data from GEO to the Earth. In the future we recommend evaluating mission data processing (MDP) solutions for both SDA and LUNINT to reduce the data load on the communication systems. Possible MDP solutions for SDA include velocity match filtering, object chipping, and observation only data. LUNINT MDP options would include real-time synchronous addition of fast frames to implement virtual TDI as described above. Also desired is change detection against stored or on-the-fly synthetic images of high-value portions of the lunar surface using the methods described in our companion paper [3].

## 7. HYBRID CASE STUDY

### 7.1 SDA Radiometric performance

The radiometric performance of the payload design was calculated for the SDA mission. Ball Aerospace's Radiometric Math Model (RMM) calculates the pixel's Signal to Noise Ratio (SNR) considering telescope, detector, and target parameters, as well as higher-order effects such as stray light and random motion jitter, among others. The model inputs jitter as a random Brownian motion process that widens the PSF at the focal plane. The effect of jitter is a reduction of the EE on the pixel and, thus, jitter degrades the pixel's SNR. Since jitter is Brownian process, its effect on the PSF increases with time. The impact on a pixel's SNR from jitter increases with longer integration times. In addition, the PSF of consecutive frames will be different depending on the amount of jitter. Therefore, jitter widens the PSF of coadded frames. This result reduces the benefits of coadding frames to improve SNR. Our model includes the variables described above, which allows us to explore the trade-space to optimize the payload's configuration in terms of integration time, number of coadded frame, etc.

Table 4: Optical and mission parameters for calculation of radiometric performance

Parameter	Value
Aperture Diameter (cm)	30
Focal Length (mm)	995.7
F/#	3.32
IFOV ( $\mu$ rad)	18.08
HFOV / VFOV (degrees)	4.24 / 2.12
EE Optics	75%
Range (km)	58,270
Solar Phase angle (degrees)	90
Integration time (s)	5

In this paper, the detector parameters of the strawman focal plane, Table 3, were utilized. The calculations assume an integration time of 5 seconds and a solar phase angle of 90 degrees. The dependence of stray light (Y-orient) on the angle from lunar limb is shown in Fig. 6. Table 3 combined with Table 4 summarizes the most relevant sensor parameters. The calculated pixel's SNR as a function of angle from lunar limb is shown in Fig. 7. For angles greater than 12 degrees, the model predicts an SNR greater than 6 (solid blue curve). For angles smaller than 12 degrees, the SNR decreases rapidly. This is consistent with the sharp increase of stray light for angles smaller than 12 degrees. Remarkably, the model captures the effect of jitter on frame coadding. Specifically, for this sensor and assumed operating conditions, frame coadding does not improve SNR as it would in a scenario without jitter. The model predicts that coadding 2 frames results in a very small improvement of SNR (dashed red curve). Furthermore, coadding more than 2 frames degrades SNR (dashed yellow curve).

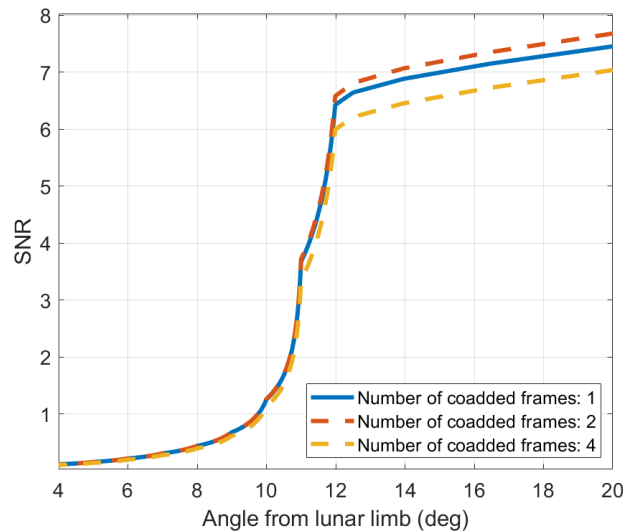


Fig. 7. Signal to noise ratio as function of angle from lunar limb

### 7.1 SDA performance against lunar target deck

As we described in [1] a majority of defined lunar orbit trajectories reside in the space between L1 and L2. Due to this, we define the SDA region of interest as an ellipsoidal volume extending 10,000 km beyond L2 (~75,000 km in either L1/L2 direction). Ten Lunar orbit families listed in Table 5 were used to evaluate the performance of a single sensor described above when their trajectories cross into the ellipsoidal volume. In the SDA performance evaluation, we assumed a 30 degree sun avoidance constraint. The MTTA for these orbital families is on average between 2-6 days with a maximum of 9.79, while the maximum revisit interval was 0.62 days as shown in Table 5.

Table 5: MTTA and average revisit intervals for lunar orbit families within ellipsoidal volume defined above

Orbit Family	Min MTTA (days)	Average MTTA (days)	Max MTTA (days)	Min Revisit Interval (days)	Average Revisit Interval (days)	Max Revisit Interval (days)
<b>Lyapunov</b>	0.015	5.88	8.44	0.046	0.28	0.45
<b>Low Prograde Western</b>	0.014	3.27	8.44	0.046	0.16	0.45
<b>Distant Prograde</b>	0.014	2.52	8.44	0.046	0.13	0.45
<b>Distant Retrograde</b>	0.014	2.29	9.76	0.046	0.13	0.60
<b>Dragonfly North</b>	0.006	2.24	9.76	0.035	0.12	0.60
<b>Butterfly North</b>	0.005	2.17	9.76	0.029	0.12	0.60
<b>Axial</b>	0.005	2.27	9.76	0.029	0.12	0.62
<b>Vertical</b>	0.005	2.30	9.76	0.029	0.13	0.62
<b>Halo North</b>	0.004	2.37	9.76	0.028	0.13	0.62
<b>Halo South</b>	0.004	2.45	9.76	0.028	0.13	0.62

## 7.2 LUNINT performance with the Hybrid Payload

The LUNINT MTTA will be similar to Case 3 from last year's paper [1]. That is, the sensor will have access to the region of interest within 5 degrees of the Pole on each orbit (period = 146 minutes), with illumination and thermal conditions dependent on topography as well as astronomy as discussed in more detail in our companion papers. The MTTA increases further from the Pole until the surface is no longer accessible, in the sense of the GSD being more than 2.0 m and hence not useful for LUNINT. This occurs at 45 degrees latitude. Of course, access to both poles in this elliptical orbit would require two vehicles in complementary orbits, as we discussed last year

## 8. CONCLUSIONS

This paper began with the hybrid space domain awareness and lunar intelligence sensor first described in last year's paper [1] and matured that concept in order to develop a telescope to meet a hybrid case study. The lunar merit function was developed to provide optimal orbit parameters depending on the preference to an SDA vs LUNINT mission. For the case study we selected a merit function that best balanced the two missions to define an orbit best supported both SDA and LUNINT. Given the goal GSD of 0.5m, target visual magnitude of 16.9, and orbit we defined a strawman FPA that would support both mission requirements. This strawman FPA could be used in discussions with potential FPA manufactures. We also investigated multiple telescope forms and selected a reflective triplet design due to its compactness and poor stray light performance. Finally, we evaluated the sensor, FPA plus telescope, performance against ten lunar orbital families and lunar surface observability. Both SDA and LUNINT mission needs were met with fast revisit intervals for SDA targets and coverage of the South pole using a single Hybrid sensor. In the future, we recommend working directly with the customer community for identifying SDA vs LUNINT preference in the merit function, updating performance calculations based on potential host or free-flyer spacecraft, and optimizing mission data processing to meet the communication limitations of those spacecraft.

## 9. REFERENCES

- [1] E.D. Silva, J.E. Van Cleve, R. Philbrick et al., Systems and Methods for Hybrid Lunar Surface and Space Domain Situational Awareness, *AMOS 2021*
- [2] D. P. Osterman, J. Van Cleve, A. M. Lawitzke et al., Anthropogenic Change Detection On and Close to the Moon for Space Domain Awareness, *AMOS 2022*
- [3] J. E. Van Cleve, D. P. Osterman, A. M. Lawitzke et al., A Year in the Life of the Shackleton Space Domain Awareness Station, *AMOS 2022*
- [4] J. B. Marion, *Classical Dynamics*, 1970

- [5] R. R. Bate, D. D. Mueller, and J. E. White. *Fundamentals of Astrodynamics*, 1971 (BMW)
- [6] A. Cota, C. J. Florio, D. J. Duvall, and M. A. Leon, The Use of the General Image Quality Equation in the Design and Evaluation of Imaging Systems, *Proc SPIE* Vol. 7458, 74580H
- [7] D. Folta and D. Quinn, Lunar Frozen Orbits, AIAA/AAS Astrodynamics Specialist Conference and Exhibit, *AIAA 2006-6749* <https://arc.aiaa.org/doi/10.2514/6.2006-6749>, 2012
- [8] J. E. Van Cleve, A. M. Lawitzke, E. MacAnlis, et al., Hiding in plain sight: observing objects in low lunar orbit and the L2 dark cone from a lunar surface observatory, *AMOS 2021*